

# Thermoelastic stress in concentrating solar receiver tubes: a retrospect on stress analysis methodology, and comparison of salt and sodium

William R. Logie\*, John D. Pye, Joe Coventry\*\*

*Solar Thermal Group, Research School of Engineering, Australian National University, Canberra, Australia*

## Abstract

Temperature distribution in nonaxisymmetrically concentrating solar thermal receivers tubes is calculated for the steady-state solution with a Gauss-Seidel iteration in cylindrical coordinates. The classical plane-biharmonic thermoelastic approach to nonaxisymmetrically heated tube stress is applied. Calculation of the dominant axial thermal stress component is included. Validation is obtained with the linear-elastic thermal stress OpenFOAM® solver. Thermoelastic stress in stainless steel 316 Schedule 5S DN25 (1") tubes containing liquid sodium is found to be 35% lower than in tubes containing molten salt. The difference is due to the higher conductivity of liquid sodium which maintains a smaller temperature difference between the front and back tube sides. A simplified thermal stress formula is shown to be erroneous if not implemented as originally documented. The sensitivity of tube thermoelastic stress to tube material and flow properties is illustrated with parameter variation, and the impact of solar concentrated heat flux is explored with some typical and ideal tube circumference flux profiles.

**Keywords:** Concentrating Solar Thermal (CST), OpenFOAM®, Fluid Structure Interaction (FSI), linear-elastic thermal stress, nonaxisymmetrically heated tubes

## 1. Introduction

Current state-of-the-art concentrating solar thermal power (CSP) tower receivers employ thin-walled stainless steel or alloy tube panels in which the chosen heat transfer fluid passes through the incident solar flux multiple times to attain the outlet temperature desirable for the selected power cycle. Receivers using molten nitrate salts have to date operated between the cold storage returned from the steam generator at 290 °C (Zavoico, 2001) and below the salt's decomposition temperature of 600 °C, or more precisely 565 °C to protect the receiver tubes from corrosion (Drake et al., 2014).

For advanced power cycles (e.g., ultra-supercritical steam and supercritical CO<sub>2</sub>), heat carrier temperatures of 700 °C and higher are pursued (Pomeroy et al., 1978; Besarati and Goswami, 2017). To power such cycles with CSP, high solar concentration ratios (power density) combined with methods of improving effective absorptance (such as by employing cavities) are required to combat the radiative losses of the receiver to the environment. Liquid metals such as lead-bismuth eutectic, tin and sodium present an enticing combination of characteristics for advanced CSP: namely, a high conductivity, a reasonable density (higher than air and steam but lower than molten salt) and a high boiling point (sodium has a liquid range 100 °C to 890 °C Romero and González-Aguilar, 2017).

A limiting factor to power density is thermal stress in the heated receiver tubes on account of the temperature difference between irradiated front and concealed back tube side, observed as a bending moment along the axial or longitudinal coordinate direction (Falcone, 1986). Repeated transitions in the magnitude of thermal stress from diurnal and cloud-transition cycling fatigues metal. Excursions in stress particularly at metal temperatures higher than half their melting point induces creep. The individual mechanisms and the interaction of creep and fatigue leads to permanent plastic deformation of the metal and eventual failure. Accounting only for diurnal creep-fatigue over a thirty-year design life, the peak allowable flux for stainless steel 316 (UNS S31600) tubes carrying sodium was predicted at 1.75 MW m<sup>-2</sup> as compared to 0.85 MW m<sup>-2</sup> for molten salt (Falcone, 1986; Kistler, 1987). The high thermal conductivity of liquid metal permits higher flux for the same allowable stresses by keeping the front side tube temperature closer to that of the back side tube temperature (Falcone, 1986).

Kistler employed approximations in his analysis relating the peak stress calculated by way of a simple Roark's formula (Young and Budynas, 2002) to the inelastic strain calculated in finite element results (Rao et al., 1979), a correlation heavily dependent on the yield stress of the tube material. His method is helpful however in working from a desired design life backwards to the heat transfer coefficient and peak flux on a given tube (Vant-Hull, 2002; Kolb, 2011; Liao et al., 2014; Luo et al., 2014), rather than the lengthy process of testing every design's fatigue life in finite element analysis.

In the determination of maximum allowable flux, some authors have implemented another Roark's formula (e.g. ex-

\*Corresponding author. Tel.: +61 2 6125 0411

\*\*Principal corresponding author. Tel.: +61 2 6125 2643

Email addresses: will.logie@anu.edu.au (William R. Logie), joe.coventry@anu.edu.au (Joe Coventry)

## Nomenclature

### Greek symbols

$\alpha$	Absorptivity	
$\beta$	Stefan-Boltzmann constant	(W m <sup>-2</sup> K <sup>-4</sup> )
$\Delta, \delta$	Difference operator	
$\epsilon$	Emissivity	
$\eta$	Thermal efficiency	
$\kappa$	Thermal diffusivity	(m <sup>2</sup> s <sup>-1</sup> )
$\lambda$	Coefficient of linear thermal expansion	(m m <sup>-1</sup> K <sup>-1</sup> )
$\mu$	Dynamic (shear) viscosity	(mPa s)
$\nabla^2$	Laplace operator	
$\nu$	Poisson's ratio	
$\rho$	Density	(kg m <sup>-3</sup> )
$\sigma$	Stress	(MPa)
$\theta$	Cylindrical coordinate	(m)

### Roman symbols

$\dot{m}$	Mass flow	(kg s <sup>-1</sup> )
$A$	Cross sectional tube area	(m <sup>2</sup> )
$a$	Tube inner radius	(m)
$A, B, C, D$	Fourier coefficients	
$b$	Tube outer radius	(m)
$c_p$	Specific heat at constant pressure	(J kg <sup>-1</sup> K <sup>-1</sup> )
$E$	Young's modulus	(GPa)
$F$	Force	(N)
$h$	Convection coefficient	(W m <sup>-2</sup> K <sup>-1</sup> )
$K$	Geometric thermal stress term	(K)
$k$	Conductivity	(W m <sup>-1</sup> K <sup>-1</sup> )
$p$	Pressure	(bar)
$q$	Sensible heat	(W)

$q''$	Normal heat flux density	(W m <sup>-2</sup> )
$R$	Thermal insulance/resistance	(m <sup>2</sup> K W <sup>-1</sup> )
$r$	Radial coordinate	(m)
$s_{ij}$	Stress deviator tensor	(MPa)
$T$	Temperature	(°C)
$U$	Bulk fluid velocity	(m s <sup>-1</sup> )
$u$	$x$ -coordinate displacement vector	(m)
$v$	$y$ -coordinate displacement vector	(m)
$w$	$z$ -coordinate displacement vector	(m)
$z$	Axial coordinate	(m)
$Bi$	Biot number	
$Nu$	Nusselt number	
$Pr$	Prandtl number	
$Re$	Reynolds number	

### Subscripts

$c$	Tube crown
$m$	Mean
$Eq$	Equivalent/von Mises
$\infty$	Ambient
$f$	Fouling
$htf$	Bulk heat transfer fluid
$inc$	Incident
$i$	Inner surface
$o$	Outer surface
$t$	Tube
$\theta$	Circumferential (hoop) component
$r$	Radial component
$z$	Axial component

ample 16, p762 Young and Budynas, 2002) which only accounts for circumferential stress under the assumption it is the same as axial stress at the extreme inner or outer tube surface (Rodríguez-Sánchez et al., 2014; Sánchez-González et al., 2017) - something only true for axisymmetrically heated tubes. Others have implemented the full set (radial, circumferential and axial) of thermoelastic stress equations for axisymmetrically heated tubes (Timoshenko and Goodier, 1951; Faupel and Fisher, 1981) and extended their analysis to include creep-fatigue (Fork et al., 2012; Neises et al., 2014; Nithyanandam and Pitchumani, 2016). Most recently Marugán-Cruz et al. (2016) implemented a biharmonic thermoelastic stress calculation for nonaxisymmetrically heated tubes (Gatewood, 1941) but bracketed axial stress from their analysis, referring the reader to the simple plane-strain equation for the axial component. Kim et al. (2016) subsequently showed how the biharmonic calculation of thermal stress for nonaxisymmetrically heated tubes results in a lower prediction of circumferential stress at the tube front side (crown) than if the axisymmetrical equations are used to predict stress for the same temperature difference observed.

Recent efforts to invigorate the use of sodium as a heat trans-

fer fluid for high temperature advanced power cycles (Boerema, 2014; Coventry et al., 2015; Logie et al., 2015, 2016) require an accurate assessment of thermal stress within a model incorporating the flow path, the panel configuration and the solar field optical accuracy. Although the finite element method (FEM) is rapidly overshadowing the utility of classical analytical methods thanks to modern computational power, parameter studies and optimisation algorithms require thousands of iterations, and therefore in preliminary design screening such analytical approaches are still useful.

Given the varied approaches to thermal stress mentioned above it was deemed necessary to revisit the classical thermoelastic approach to nonaxisymmetrically heated tube stress with an emphasis on the calculation of the axial component. The significant biharmonic contributions are unified within a Python code<sup>1</sup> and validation is provided with results generated in an OpenFOAM<sup>®</sup> linear-elastic thermal stress solver (Tuković et al., 2014)<sup>2</sup>.

The benefit of using liquid sodium over molten salt in reduc-

<sup>1</sup><https://github.com/willietheboy/nashTubeStress>

<sup>2</sup><https://github.com/wyldckat/FluidStructureInteraction>

ing thermoelastic tube stress is shown for DN25 (1") Schedule 5S UNS S31600 (stainless steel 316) tubes. Ways to mitigate thermoelastic stress are illustrated with parameter variation of tube and fluid flow properties, and under several idealised flux distributions.

## 2. Methodology

The approach to modelling a receiver tube is to consider it as a series of finite cylindrical segments with inner radius  $a$  and outer radius  $b$  where the temperature of each tube segment is assumed to vary in the radial  $r$  and angular coordinate  $\theta$  but not axially  $z$ . Given that the collimated solar flux is symmetrical about the  $\theta = 0^\circ, 180^\circ$  axis, only half of a cylindrical coordinate system was implemented as illustrated in Fig. 1.

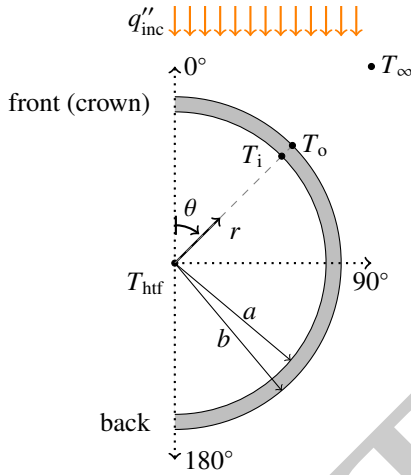


**Fig. 1:** Cross-section of a nonaxisymmetrically irradiated tube given the assumption that collimated solar flux  $q''_{inc}$  is symmetrical about  $\theta = 0^\circ, 180^\circ$  and that only half the tube circumference needs modelled

### 2.1. Temperature field

It assumed that the temperature distribution reaches its steady-state and can be found by way of the Laplace equation in cylindrical coordinates Eq. (1).

$$\nabla^2 T(r, \theta) = \frac{1}{r} \frac{\partial}{\partial r} \left( r \frac{\partial T}{\partial r} \right) + \frac{1}{r^2} \frac{\partial^2 T}{\partial \theta^2} = 0 \quad (1)$$

For simple boundary conditions (i.e. specified temperature, convection coefficient or heat flux) the separation of variables or Fourier method can provide solutions to such two or three dimensional steady-state problems algebraically, however where mixed boundary conditions are to be implemented solutions using this mathematical tool are not easy to obtain (Boley and Weiner, 1960; Hetnarski and Eslami, 2009). For this reason the Gauss-Seidel iterative method was implemented (Kiusalaas, 2010). Ghost nodes were introduced beyond the symmetry boundary nodes to mirror the first nodes inside the mesh.

#### 2.1.1. Outer thermal boundary condition

To simulate the gain from collimated flux and loss to the environment from radiation and convection a Neumann boundary condition was applied to the outer tube surface,

$$k_t \left. \frac{\partial T}{\partial r} \right|_{r=b} = - \begin{cases} \alpha q''_{inc} \cos(\theta) & : 0 \leq \theta \leq 90^\circ \\ 0 & : \text{otherwise} \end{cases} + \epsilon \beta (T_o^4 - T_\infty^4) + h_o (T_o - T_\infty) \quad (2)$$

where  $k_t$  is the tube conductivity, an  $\alpha$  of 0.97 (Pye et al., 2014) and  $\epsilon$  of 0.87 (Ho et al., 2013) represent Pyromark 2500<sup>®</sup> absorptivity and emissivity respectively,  $q''_{inc}$  is the incident (concentrated) solar flux,  $\beta$  is the Stefan-Boltzmann constant and  $h_o$  is the outer convection coefficient. A constant overall external convection loss  $h_o$  of  $30 \text{ W m}^{-2} \text{ K}^{-1}$  was considered (Siebers and Kraabel, 1984; Pye et al., 2014), which accounts for considerable wind<sup>3</sup>.

#### 2.1.2. Inner thermal boundary condition

To simulate forced convection to molten salt or liquid sodium a Neumann boundary condition was applied to the inner tube surface:

$$k_t \left. \frac{\partial T}{\partial r} \right|_{r=a} = h_i (T_i - T_{htf}) \quad (3)$$

The inner convective heat transfer coefficient was evaluated with Nusselt correlations by way of bulk flow velocity  $U$  and Reynolds Number using temperature dependent thermo-physical properties (density  $\rho$ , specific heat  $c_p$ , molecular viscosity  $\mu$  and thermal conductivity  $k$ ) for molten salt (Zavoico, 2001) and liquid sodium (Fink and Leibowitz, 1995):

$$U = \frac{\dot{m}}{\pi a^2 \rho} \quad (4)$$

$$\text{Re} = \frac{\rho U 2a}{\mu} \quad (5)$$

For liquids with a Prandtl number (Pr) of 0.7 to 16 700 the impact of temperature difference in the thermal boundary can be captured in the ratio of bulk fluid to inner tube wall molecular viscosity by way of the Sieder and Tate correlation (Incropera et al., 2006) with all properties other than  $\mu_i$  evaluated at the bulk fluid temperature:

$$\text{Nu} = 0.027 \text{Re}^{\frac{4}{5}} \text{Pr}^{\frac{1}{3}} \left( \frac{\mu_{htf}}{\mu_i} \right)^{0.14} \quad 0.7 < \text{Pr} < 16700 \quad (6)$$

Or disregarding the thermal boundary layer (viscosity ratio) with the Dittus-Boelter equation:

$$\text{Nu} = 0.023 \text{Re}^{\frac{4}{5}} \text{Pr}^{0.3} \quad 0.7 < \text{Pr} < 16700 \quad (7)$$

Concealed in both Eqs. (6) and (7) is the assumption that the ratio of hydrodynamic to thermal diffusivity (Pr) is independent of flow condition and distance from wall. Liquid metals, however, have a high thermal conductivity and very low

<sup>3</sup>The case of no wind is closer to  $10 \text{ W m}^{-2} \text{ K}^{-1}$ .

Prandtl number ( $Pr \approx 0.01$  or less), which means that the thermal boundary layer is much thicker than the hydrodynamic boundary layer and is characterised by molecular conduction until  $Re > 2.14 \times 10^5$  (Pacio et al., 2015). The assumption of the Reynolds analogy - that the turbulent Prandtl number  $Pr_t$  is constant and close to unity - cannot be applied, and while a number of empirical and semi-empirical models for  $Pr_t$  have been adapted for use with the Lyon-Martinelli correlation, they result in significant variance of  $Pr_t$  1 to 2.5 and thus reduction in  $Nu$  for a given  $Re$ . Short of computational fluid dynamics (CFD) (Marocco et al., 2016) the most fitting correlation evaluated by Pacio et al. (2015) - the Skupinski, Tortel and Vautrey (1965) - was used with properties evaluated at the bulk fluid temperature:

$$Nu = 4.82 + 0.0185 (Re Pr)^{0.827} \quad (8)$$

which is valid for Reynolds numbers up to  $\approx 1 \times 10^6$ .

Fouling resistance  $R_f$  could be added to the convective heat transfer coefficient  $h_i$  according to Eq. (10) if enough confidence were obtained in its quantity:

$$h_i = \frac{Nu k_{htf}}{2a} \quad (9)$$

$$\frac{1}{h_{f,i}} = R_f + \frac{1}{h_i} \quad (10)$$

Rodríguez-Sánchez et al. (2014) gives the fouling factor  $R_f$  for molten salt as  $8.808 \times 10^{-5} \text{ m}^2 \text{ K W}^{-1}$ , which is the same value given by Zavoico (2001) ( $5 \times 10^{-4} \text{ ft}^2 \text{ }^\circ\text{F hr btu}^{-1}$ ) and is very close to that used for pipes carrying steam (Holman, 1997). The *Sodium-NaK Engineering Handbook* (Foust, 1972, Vol. 2, p292) mentions fouling in regard to steam generators as having resistance  $2.5 \times 10^{-4}$  to  $3 \times 10^{-4} \text{ ft}^2 \text{ }^\circ\text{F hr btu}^{-1}$  ( $4.4 \times 10^{-5} \text{ m}^2 \text{ K W}^{-1}$  to  $5.28 \times 10^{-5} \text{ m}^2 \text{ K W}^{-1}$ ), however being a lumped value it is uncertain to what degree this refers to the sodium or steam side of the heat exchanger. Fouling is largely a deposition of eroded or corroded solubles in heat exchangers. In the case of liquid sodium it is supposedly negligible if impurities such as oxygen are kept below a few ppm (Pacio et al., 2013). For the investigations presented here the impact of fouling was ignored however its impact is illustrated in the fluid flow sensitivity studies in Sec. 5.1.

Where appropriate the Biot number as defined in Marugán-Cruz et al. (2016) is given to express the ratio of radial to circumferential heat transfer, or in other words an indication of how axisymmetrical the heating condition is:

$$Bi = \frac{(b-a) h_i}{k_t} \quad (11)$$

Marugán-Cruz et al. show that applying the axisymmetrical thermoelastic equations (Faupel and Fisher, 1981) to the non-axisymmetrical case (Gatewood, 1941) is a reasonable approximation when  $Bi > 10$ , a questionable approximation when  $0.3 \leq Bi \leq 10$ , and qualitatively wrong when  $Bi \leq 0.3$ .

## 2.2. Thermal stress

It is important to identify the thermal expansion occurring which leads to thermal stress in CSP receiver tubes. A cube of

metal unconstrained on all sides and subject to a homogeneous change in temperature will not experience any thermal stress. The body expands and contracts linearly in all directions according to the constant change in temperature. It is only when the temperature of a continuous body varies and these different temperatures lead to nonuniform thermal expansion in respective regions of the same body that stress is observed between these regions. The resulting stress is said to be self-limiting. The change in temperature from nighttime cold-state up to operating temperature results in growth of the tube in all directions but does not result in thermal stress within the tube<sup>4</sup>.

The temperature difference from the condition of heating due to solar input during operation results in an increase in tube temperatures above the established operating or 'stress free' temperature  $T_0$ . If the axial thermal expansion of any increase in tube temperature above the stress free temperature was not allowed to happen then we would have a case of zero axial displacement, often referred to as the 'simple plane strain state'. The 'generalised plane strain state' is one in which the tube is free to expand and contract in the axial direction by a constant axial strain such that net axial force is zero. Compression is observed in the tube cross section where tube temperature is above the tube cross section's average and tension is observed where tube cross-section's temperature is below it. Axial stress arising from the nonuniform thermal expansion of receiver tube panels is normally managed via bends at the tube ends with oblique attachment to the manifold (Chavez and Smith, 1992; Winter et al., 1991). The resultant net axial stress is assumed to be zero because the tension and compression balance out, however this ignores that the bend acts as a spring when the axial expansion or contraction of any one tube differs in relation to the majority of other tubes in the panel (Narayanan et al., 1979).

The synthesised method presented here uses the approximation of two-dimensional thermoelasticity (Timoshenko and Goodier, 1951; Boley and Weiner, 1960; Hetnarski and Eslami, 2009). The articles from Goodier (1957) and Bijlaard et al. (1968) offer additional insight into the biharmonic calculation of axial stress given the generalised plane-strain state. Calculation of the radial and circumferential stress components is first presented and then calculation of the axial stress component is given for the state of zero axial displacement, zero axial force and zero axial force with annulled bending moment.

With two-dimensional steady-state heat flow established from Eqs. (1) to (3), the cylindrical thermoelastic stress components may be found by superposition of axisymmetrical and nonaxisymmetrical contributions. To this end it is convenient to separate cylinder temperatures into their geometrical average (axisymmetrical) and circumferentially varying (nonaxisymmetrical, asymmetrical or nonuniform) parts. As is customary, the expression for average geometrical surface temper-

<sup>4</sup>Though important, we neglect transient effects during receiver filling and emptying (Pacheco et al., 1995)



atures for a complete circumference are:

$$\bar{T}_i = \frac{1}{2\pi} \int_0^{2\pi} T_i d\theta \quad (12)$$

$$\bar{T}_o = \frac{1}{2\pi} \int_0^{2\pi} T_o d\theta \quad (13)$$

The circumferentially varying temperature expression can be defined by subtracting the symmetrical (logarithmic) part from the total temperature and referencing in relation to the average outer tube surface temperature as an ‘excess’:

$$T_\theta = T - (\bar{T}_i - \bar{T}_o) \frac{\ln \frac{b}{r}}{\ln \frac{b}{a}} - \bar{T}_o \quad (14)$$

Remembering that the circumferentially varying temperature distribution is steady-state, a plane harmonic Fourier series exists with radial dependent functions satisfying Eq. (1):

$$T_\theta = \sum_{n=1}^{\infty} (A_n r^n + B_n r^{-1}) \cos n\theta + (C_n r^n + D_n r^{-1}) \sin n\theta \quad (15)$$

In a single or multiply connected body, free of all surface tractions, body forces, and surfaces of displacement discontinuity, a temperature distribution which is linear (with respect to a rectangular Cartesian system) produces no stresses (Boley and Weiner, 1960). Thus, terms relating to  $r \cos \theta$  and  $r \sin \theta$  in Eq. (15) do not produce any thermal stress, and as such only  $B_n$  and  $D_n$  coefficients appear in the formulas for the thermal stress components. In addition, the so-called Michell continuity conditions<sup>5</sup> arise only for temperature terms of  $n = 0$  and  $n = 1$  (Boley and Weiner, 1960). The result is that only terms of a plane-harmonic temperature distribution for which  $n = 0$  and  $n = 1$  contribute to the stress components in the plane. Timoshenko and Goodier (1951) arrive at the same conclusion but by means of the method of complex variables, explaining more intuitively that the net heat flow associated with terms  $\cos 2\theta$ ,  $\sin 2\theta$  and greater is zero. It follows that if the temperature distribution is symmetrical about the  $\theta = 0, \pi$  axis, only cosine terms and thus  $B_1$  is required.

One method of determining the coefficients in Eq. (15) is by using a least-squares fitting algorithm<sup>6</sup>. Given the harmonic steady-state condition, the effort required in minimising the sum (integral) of the squares of the differences over the entire cross sectional area of the tube can be reduced by seeking Fourier series of Eq. (15) only at  $a$  and  $b$ :

$$T_i = \bar{T}_i + \sum_{n=1}^{\infty} B'_n \cos n\theta + D'_n \sin n\theta \quad (16)$$

$$T_o = \bar{T}_o + \sum_{n=1}^{\infty} B''_n \cos n\theta + D''_n \sin n\theta \quad (17)$$

Irrespective of the way in which the temperature distribution is described, the stress resulting from the condition of nonaxisymmetrical heating is given by:

$$\sigma_r = K \frac{\lambda E}{2(1-\nu)} \left[ -\ln \frac{b}{r} - \frac{a^2}{b^2 - a^2} \left( 1 - \frac{b^2}{r^2} \right) \ln \frac{b}{a} \right] + K_\theta \frac{\lambda E}{2(1-\nu)} \left( 1 - \frac{a^2}{r^2} \right) \left( 1 - \frac{b^2}{r^2} \right) \quad (18)$$

$$\sigma_\theta = K \frac{\lambda E}{2(1-\nu)} \left[ 1 - \ln \frac{b}{r} - \frac{a^2}{b^2 - a^2} \left( 1 + \frac{b^2}{r^2} \right) \ln \frac{b}{a} \right] + K_\theta \frac{\lambda E}{2(1-\nu)} \left( 3 - \frac{a^2 + b^2}{r^2} - \frac{a^2 b^2}{r^4} \right) \quad (19)$$

where  $E$  is the tube Young’s modulus,  $\lambda$  is its linear coefficient of thermal expansion,  $\nu$  is Poisson’s ratio and  $K$  is used to describe the various axisymmetrical and nonaxisymmetrical geometrical temperature contributions.

The contribution of  $n = 0$  to stress is from the average surface temperature difference:

$$K = \frac{\bar{T}_i - \bar{T}_o}{\ln \frac{b}{a}}, \quad (20)$$

The contribution of  $B_1$  and  $D_1$  to principal stress components using coefficients determined with Eq. (15) are:

$$K_\theta = \frac{r}{a^2 + b^2} (B_1 \cos \theta + D_1 \sin \theta) \quad (21)$$

or using coefficients determined with Eqs. (16) and (17):

$$K_\theta = \frac{rab}{b^2 - a^2} \left[ \left( \frac{B'_1 b - B''_1 a}{a^2 + b^2} \right) \cos \theta + \left( \frac{D'_1 b - D''_1 a}{a^2 + b^2} \right) \sin \theta \right] \quad (22)$$

If required<sup>7</sup>, the contribution of  $B_1$  and  $D_1$  to in-plane shear stress:

$$\sigma_{r\theta} = \tau_{r\theta} = K_\tau \frac{\lambda E}{2(1-\nu)} \left( 1 - \frac{a^2}{r^2} \right) \left( 1 - \frac{b^2}{r^2} \right) \quad (23)$$

can be found using coefficients determined with Eq. (15):

$$K_\tau = \frac{r}{a^2 + b^2} (B_1 \sin \theta - D_1 \cos \theta) \quad (24)$$

or using coefficients determined with Eqs. (16) and (17):

$$K_\tau = \frac{rab}{b^2 - a^2} \left[ \left( \frac{B'_1 b - B''_1 a}{a^2 + b^2} \right) \sin \theta - \left( \frac{D'_1 b - D''_1 a}{a^2 + b^2} \right) \cos \theta \right] \quad (25)$$

If the tube were axially constrained, the axial stress would be calculated using the simple plane strain equation with reference to the stress free temperature  $T_0$ . From Hooke’s law, for  $\epsilon_z = 0$ , we have:

$$\sigma_z = \nu(\sigma_r + \sigma_\theta) - \lambda E(T - T_0) \quad (26)$$

<sup>5</sup>The two-dimensional elastic equations were originally derived by Michell (1899) without recourse to the reduced three-dimensional compatibility equations.

<sup>6</sup>e.g. [scipy.optimize.curve\\_fit](#)

<sup>7</sup>In the case considered in-plane shear stress is less than 1% of equivalent stress.

Equation (26) can also be re-written in its stress-strain relation as:

$$\epsilon_z = \frac{1}{E} [\sigma_z - \nu(\sigma_r + \sigma_\theta)] + \lambda(T - T_0) \quad (27)$$

Given the assumption of zero axial force, the integration of axial stress  $\sigma_z$  over the tube's cross sectional area should vanish:

$$F_z = \int_A \sigma_z dA = 0 \quad (28)$$

and the integration of Eq. (27) becomes:

$$E\epsilon_z = -\nu(\bar{\sigma}_r + \bar{\sigma}_\theta) + \lambda E(\bar{T} - T_0) \quad (29)$$

where:

$$\bar{\sigma}_r = \frac{1}{A} \int_A \sigma_r dA \quad \bar{\sigma}_\theta = \frac{1}{A} \int_A \sigma_\theta dA \quad \bar{T} = \frac{1}{A} \int_A T dA \quad (30)$$

When external mechanical loads are zero ( $\bar{\sigma}_r = \bar{\sigma}_\theta = 0$ ), the axial stress is given by the generalised plane strain equation:

$$\sigma_z = \nu(\sigma_r + \sigma_\theta) + \lambda E(\bar{T} - T) \quad (31)$$

Equation (31) can be used given prior calculation of the radial and circumferential stress fields with Eqs. (18) and (19). However, in some circumstances it is convenient to calculate axial stress independently of the radial and circumferential components. Substituting Eqs. (18) and (19) into Eq. (31) results in:

$$\sigma_z = K \frac{\lambda E}{2(1-\nu)} \left[ 1 - 2 \ln \frac{b}{r} - \frac{2a^2}{b^2 - a^2} \ln \frac{b}{a} \right] + K_\theta \frac{\lambda E \nu}{1-\nu} \left( 2 - \frac{a^2 + b^2}{r^2} \right) - \lambda E T_\theta \quad (32)$$

Goodier (1957) presents in his discussion of axial stress the interesting state of zero axial force with annulled bending moment, for example where a tube is only fixed at one end. Equation (32) then becomes:

$$\sigma_z = K \frac{\lambda E}{2(1-\nu)} \left[ 1 - 2 \ln \frac{b}{r} - \frac{2a^2}{b^2 - a^2} \ln \frac{b}{a} \right] + K_\theta \frac{\lambda E \nu}{1-\nu} \left( 2 - \frac{a^2 + b^2}{r^2} \right) + \lambda E K_M - \lambda E T_\theta \quad (33)$$

where the additional term  $K_M$  expressing annulment of moment is described here with coefficients determined from Eqs. (16) and (17):

$$K_M = r \left[ \left( \frac{B'_1 a + B'_1 b}{a^2 + b^2} \right) \cos \theta + \left( \frac{D'_1 a + D'_1 b}{a^2 + b^2} \right) \sin \theta \right] \quad (34)$$

For thin shells,  $\sigma_z$  can be obtained with reasonable accuracy using the approximation from Goodier (1957):

$$\sigma_z = K_\theta \frac{\lambda E \nu}{1-\nu} \left( 2 - \frac{a^2 + b^2}{r^2} \right) + \lambda E(\bar{T} - T) \quad (35)$$

### 2.3. Pressure stress

In conjunction with thermal stress the effect of internal pressure (Timoshenko and Goodier, 1951) on an axially unconstrained tube can be similarly superimposed:

$$\sigma_r = \frac{p_i a^2}{b^2 - a^2} \left( 1 - \frac{b^2}{r^2} \right) \quad (36)$$

$$\sigma_\theta = \frac{p_i a^2}{b^2 - a^2} \left( 1 + \frac{b^2}{r^2} \right) \quad (37)$$

$$\sigma_z = \frac{p_i a^2}{b^2 - a^2} \quad (38)$$

The effect of pressure will first be considered in the sensitivity studies in Sec. 5.1.

### 3. Simplified one-dimensional methodology

A simplified approach originally introduced by Babcock & Wilcox (1984) and later used by Kistler (1987); Kolb (2011) assumes one-dimensional heat transfer through a thin-walled tube and seeks temperatures for the tube front ( $\theta = 0^\circ$ , referred to by Babcock & Wilcox as crown) assuming a half cosine flux distribution:

$$T_{c,i} = T_{htf} + \frac{\alpha q''_{inc} \frac{b}{h_i}}{h_i} \quad (39)$$

$$T_{c,o} = T_{c,i} + \alpha q''_{inc} \frac{b}{k_t} \ln \frac{b}{a} \quad (40)$$

The mean tube temperature can be derived as:

$$T_m = T_{htf} + \frac{1}{\pi} (T_{m,c} - T_{htf}) \quad (41)$$

where the mean crown temperature is given as:

$$T_{m,c} = \frac{T_{c,i} + T_{c,o}}{2} \quad (42)$$

Ignoring the effect of tube size, cross-sectional shape and wall thickness, the impact of a temperature gradient across a tube cross-section or depth<sup>8</sup>:

$$\sigma_1 = \lambda E(T_{m,c} - T_m) \quad (43)$$

and for a temperature difference across a tube wall<sup>9</sup>:

$$\sigma_2 = \lambda E \left( \frac{T_{c,o} - T_{c,i}}{2(1-\nu)} \right) \quad (44)$$

is combined into Eq. (45) to generally express the temperature differences between one part of the tube and another which contribute to thermal stress:

$$\sigma_{(1+2)} = \lambda E \left[ (T_{m,c} - T_m) + \left( \frac{T_{c,o} - T_{c,i}}{2(1-\nu)} \right) \right] \quad (45)$$

<sup>8</sup>A longitudinal slit is cut and the tube is uncurled; temperature varies from the line along the middle of the uncurled plate to the outer (slit) edge (e.g. example 13, p761 Young and Budynas, 2002).

<sup>9</sup>A simplification of the axisymmetric approach; extreme 'fibre' stress for a uniform temperature difference between inside and outside surface of a thin-walled tube (e.g. example 15, p762 Young and Budynas, 2002).

While Eq. (45) does not follow traditional yield surface criterion, [Babcock & Wilcox](#) claimed that prediction of stress with Eq. (45) is within 3% accuracy of FEM when tubes are not axially joined by a membrane, and that Eq. (45) overpredicts FEM by 10% if a membrane is employed<sup>10</sup>. [Kistler](#) applies a correlation for comparing this stress/strain to results obtained in finite element predictions, however it is unclear how it relates to an equivalent or Mises criterion. [Kolb](#) applies Eq. (45) without correction.

The simplification employed in Eq. (45) becomes more evident with recognition of [Goodier \(1937a,b\)](#). Applying biharmonic thermoelastic stress analysis to thin-shell theory, [Goodier](#) showed that the nonaxisymmetrical extreme fibre stresses can be predicted ignoring tube geometry using the Fourier coefficients determined for Eqs. (16) and (17). The extreme outer longitudinal or axial fibre stress at the crown is thus given by:

$$\sigma_z = \lambda E \left[ -\frac{1}{2}(T_i + T_o) + \frac{1}{2}(T_i - T_o) + \frac{1}{2}(\bar{T}_i + \bar{T}_o) \right] \quad (46)$$

and the extreme outer circumferential fibre stress at the crown by:

$$\sigma_\theta = \frac{\lambda E}{2(1-\nu)} \left[ (\bar{T}_i - \bar{T}_o) + \sqrt{(B_1'' - B_1')^2 + (D_1'' - D_1')^2} \right] \quad (47)$$

This somewhat defeats the purpose of a simplified one-dimensional method as determination of Fourier coefficients by approximation or as presented in Sec. 2 is required and any improvement in component stress accuracy does not outweigh the added effort, given the persisting reliance on one-dimensional heat transfer and thin-shell theory.

#### 4. Validation

Equivalent or von Mises stress<sup>11</sup> is calculated from Cartesian coordinates in OpenFOAM<sup>®</sup> by way of the stress deviator tensor  $s_{ij}$  with Eq. (48):

$$\sigma_{Eq} = \sqrt{\frac{3}{2} s_{ij} s_{ij}} \quad (48)$$

or in cylindrical coordinates from the present method with Eq. (49) where  $\tau_{rz} = \tau_{z\theta} = 0$  due to the assumption of generalised plane-strain:

$$\sigma_{Eq} = \sqrt{\frac{[(\sigma_r - \sigma_\theta)^2 + (\sigma_\theta - \sigma_z)^2 + (\sigma_z - \sigma_r)^2]}{2} + 6\tau_{r\theta}^2} \quad (49)$$

For plotting of principal stress components the symmetrical Cartesian stress tensor calculated in OpenFOAM<sup>®</sup> was translated to cylindrical coordinates.

Validation of the Laplace solution in OpenFOAM<sup>®</sup> requires a fine radial discretisation for temperature field interpolation<sup>12</sup>, whereas solid mechanics prefers cells with minimum skew and aspect ratios close to unity. To avoid convolution of thermal and solid mechanics discretisation and modelling error between OpenFOAM<sup>®</sup> models and Python code, validation cases with analytical temperature distributions were sought. The first is from [Timoshenko and Goodier](#) (case 135, p412 1951) for axisymmetrically heated tubes, and the second is the nonaxisymmetrical temperature distribution from [Holms \(1952\)](#) later used by [Bijlaard et al. \(1968\)](#) and [Gupta et al. \(1978\)](#). Given the occurrence of both imperial and SI units in the above mentioned works, results are plotted showing stress and dimension in both units. The boundary conditions used in the OpenFOAM<sup>®</sup> models are summarised in Table 1.

**Tab. 1:** OpenFOAM<sup>®</sup> displacement boundary condition summary

Boundary	OpenFOAM <sup>®</sup>
$r = a$	tractionDisplacement pressure = $p_i$
$r = b$	tractionDisplacement pressure = 0
$\theta = 0, \pi$	symmetryPlane
$\pm z$	directionMixedDisplacement valueFraction = (0 0 0 0 0 1) refGradient = (0 0 0) refValue = (0 0 $w$ )

The constant axial displacement applied to either end of the tube depends on whether we seek a simple plane strain (zero axial displacement) or generalised plane strain (zero axial force) state. The former has displacement  $w = 0$  enforced and the latter requires a constant axial strain  $\epsilon$  or displacement  $w$  according to Hooke's Law where the sign of  $\int_A \sigma_z dA$  determines the direction of displacement:

$$\epsilon_z = \frac{F_z}{EA} \quad (50)$$

$$w = \frac{\int_A \sigma_z dA z}{EA} \quad (51)$$

Some modification of the standard direction-mixed-displacement boundary condition would be required to allow for dynamic in-simulation adjustment, however one can first run a simulation of the simple plane strain case and subsequently work out via Eq. (51) the displacement required for annulled axial force.

##### 4.1. Axisymmetrically heated tubes

As in [Timoshenko and Goodier](#) (case 135, p412 1951), a condition of heating is set up in a 'cylinder with a concentric circular hole' with a uniform inside temperature  $T_i$  of 0 °C and

<sup>10</sup>Note that [Bijlaard et al.](#) addressed this some years prior.

<sup>11</sup>To get a feel for equivalent stress: if we place the same metal cube from Sec. 2.2 at the bottom of the ocean it will experience the same force on all sides and thus stress in all orthogonal coordinate directions. In such a situation no equivalent stress is observed and the cube could be as deep as it likes without ever yielding.

<sup>12</sup>Particularly at surfaces/boundaries where a Neumann gradient condition is imposed.

a uniform outside temperature  $T_o$  of 100 °C and representative tube properties given in Table 2.

**Tab. 2:** Properties for Timoshenko and Goodier (case 135, p412 1951)

Property	Units	Value
$E$	GPa	200
$\lambda$	$10^{-5} \text{ m m}^{-1} \text{ K}^{-1}$	1
$\nu$		0.3
$a$	mm	500
$b$	mm	700

The temperature distribution is taken to be symmetrical about the axis (axisymmetric) and independent of axial coordinate  $z$ . The radial temperature distribution is calculated accordingly:

$$T = (T_o - T_i) \frac{\ln \frac{r}{a}}{\ln \frac{b}{a}} \quad (52)$$

The OpenFOAM® model could be made axisymmetrically (as a wedge) but for illustration purposes a four metre length of a quarter tube circumference was modelled. Figure 2 shows an exaggeration of the displacement in the quarter-tube OpenFOAM® model when the ends are axially constrained (Fig. 2a) or in axial equilibrium (Fig. 2b).

Figure 3 shows component stress and a comparison of analytical equivalent stress against results sampled from the OpenFOAM® model.

The condition of constrained tube ends results in the largely compressive axial stress  $\sigma_z$  becoming the dominant component in the equivalent stress criterion  $\sigma_{Eq}$  (Fig. 3a). The notion that axial stress can be ignored in nonaxisymmetrically heated tubes (Rodríguez-Sánchez et al., 2014; Marugán-Cruz et al., 2016; Sánchez-González et al., 2017) possibly comes from the awareness that under the axisymmetrical heating condition unconstrained tubes have axial stress more-or-less equal in magnitude and character to hoop stress (Fig. 3b).

#### 4.2. Nonaxisymmetrically heated tubes

We mention in Sec. 4.1 that significantly more symmetry exists than we used for illustration. Proper application of Eq. (51) in the OpenFOAM® model allows one to reduce the axial mesh resolution to one cell<sup>13</sup>. This results in a significant reduction in calculation time. In the case of nonaxisymmetrically heated tube we are required to model half a tube cross section if its temperature distribution is symmetrical about the  $\theta = 0, \pi$  axis, or the complete tube cross section if the temperature distribution is otherwise irregular.

The temperature distribution from Holms (1952) consists of a symmetrical temperature difference of 0°F on the inside and

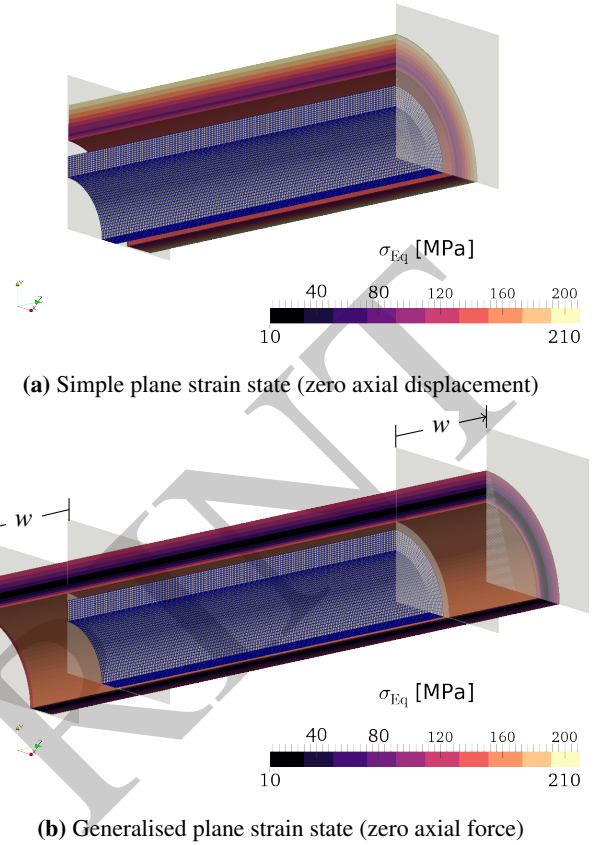


**Fig. 2:** Timoshenko and Goodier (case 135, p412 1951); original mesh shown inside and a warped mesh  $(u, v, w) \times 1000$  outside showing equivalent stress  $\sigma_{Eq}$  and the result of (a) axially constrained ends and (b) axially free ends.

500°F on the outside, and a circumferentially varying temperature difference of 0°F on the inside and  $1000^\circ\text{F} \cos \theta$  on the outside. The temperature differences being of interest, an expression for temperature distribution with conversion to SI units is given in Eq. (53) and for tube properties in Table 3.

$$T = \frac{555.56 b}{b^2 - a^2} \frac{r^2 - a^2}{r} \cos \theta + 277.78 \left( 1 - \frac{\ln \frac{b}{r}}{\ln \frac{b}{a}} \right) \quad (53)$$

**Tab. 3:** Tube properties and radii from Holms (1952)

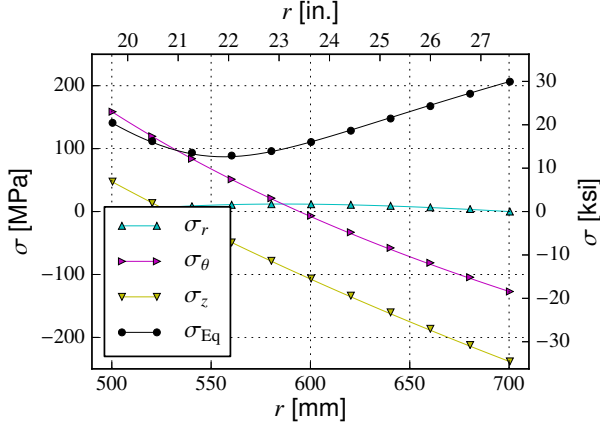
Property	Units	Value
$E$	GPa	120.66
$\lambda$	$10^{-6} \text{ m m}^{-1} \text{ K}^{-1}$	14.4
$\nu$		0.3
$a$	mm	101.6
$b$	mm	304.8

A visualisation of the temperature distribution on the OpenFOAM® mesh is given in Fig. 4.

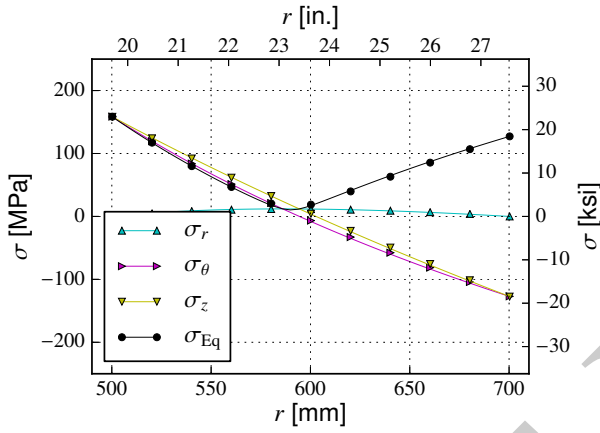
Figure 5 shows a comparison of analytical stress components against results sampled from the OpenFOAM® model.

<sup>13</sup>Plane stress problems can be handled in OpenFOAM® in this manner but only where external loads are applied. Due to the Finite Volume Method (FVM) solver construction, thermal expansion in the  $z$ -axis cannot be suppressed and a plane stress solution cannot exist. This is desirable and mentioned here only for clarity.





(a) Simple plane strain state (zero axial displacement)



(b) Generalised plane strain state (zero axial force)

**Fig. 3:** Timoshenko and Goodier (case 135, p412 1951); sample of component and equivalent stresses through the tube; solid lines denote results from Eqs. (18), (19) and (32) and markers denote results sampled from the OpenFOAM® model; compression is negative and tension is positive

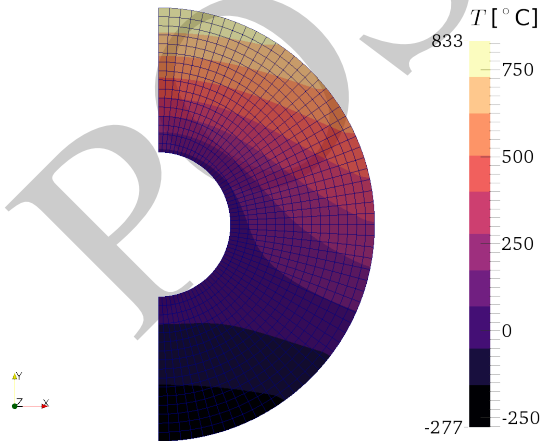


**Fig. 4:** OpenFOAM® mesh for Holms (1952) showing the temperature distribution from Eq. (53)

Agreement is very good, particularly at the symmetry plane  $\theta = 0^\circ, 180^\circ$ . Some discrepancy is observed in Figs. 5a and 5c at angles  $\theta = 60^\circ, 120^\circ$ . Increasing the mesh density beyond that shown in Fig. 4 resulted in a negligible improvement in the agreement between analytical and OpenFOAM® results.

The impact these discrepancies have on equivalent stress observed where peak stress occurs in nonaxisymmetrically heated tubes at  $\theta = 0^\circ$  in Fig. 6 is negligible.

The works which have served for validation (Holms, 1952; Bijlaard et al., 1968; Gupta et al., 1978) only illustrate their results for circumferential stress. Given our intended purpose in the analysis of thin-walled tubes, the above validation is encouraging and suggests that the small discrepancy could be reduced with further refinement of the numerical finite volume method (FVM) model. To what extent we are observing a discrepancy due to the two-dimensional approximation of thermoelasticity used in derivation of the analytical equations was not investigated.

## 5. Results & Discussion

A bulk fluid temperature of  $450^\circ\text{C}$  was chosen for the following comparisons between molten nitrate salt and liquid sodium, and DN25 Schedule 5S UNS S31600 (stainless steel 316) was selected as a representative panel tubing material. UNS S31600 is Boiler and Pressure Vessel Code (BPVC) approved for service with sodium at elevated temperatures (Section III, Subsection NH ASME, 2007) and is readily available with a wall thickness of 1.65 mm in the nominal diameter range from DN15 up to DN50. The relevant material properties and tube dimensions are given in Table 4, and a summary of the flow properties of salt (Zavoico, 2001) and sodium (Fink and Leibowitz, 1995) for DN25 with a bulk fluid temperature of  $450^\circ\text{C}$  is given in Table 5. The flow rates were chosen to reflect representative bulk tube velocities with a similar pressure drop  $\Delta p^{14}$ . The analytical method presented in Sec. 2 is used throughout.

**Tab. 4:** UNS S31600 DN25 Sch. 5S tube properties at a bulk fluid temperature of  $450^\circ\text{C}$  (Section II, Part D, Subpart 2 ASME, 2007)

Property	Units	Value
$k_t$	$\text{W m}^{-1} \text{K}^{-1}$	20
$E$	GPa	165
$\lambda$	$10^{-6} \text{ m m}^{-1} \text{K}^{-1}$	18.5
$\nu$		0.3
$a$	mm	15.049
$b$	mm	16.7

Figures 7 and 8 are colour-maps generated with the present method showing temperature and equivalent tube stress respectively for molten salt and liquid sodium tubes irradiated with  $850 \text{ kW m}^{-2}$ . The tube's maximum temperature and stress on

<sup>14</sup>It is understood that other comparison metric exist which are bracketed in the present work, e.g., volumetric heat capacity  $\rho c_p$ .

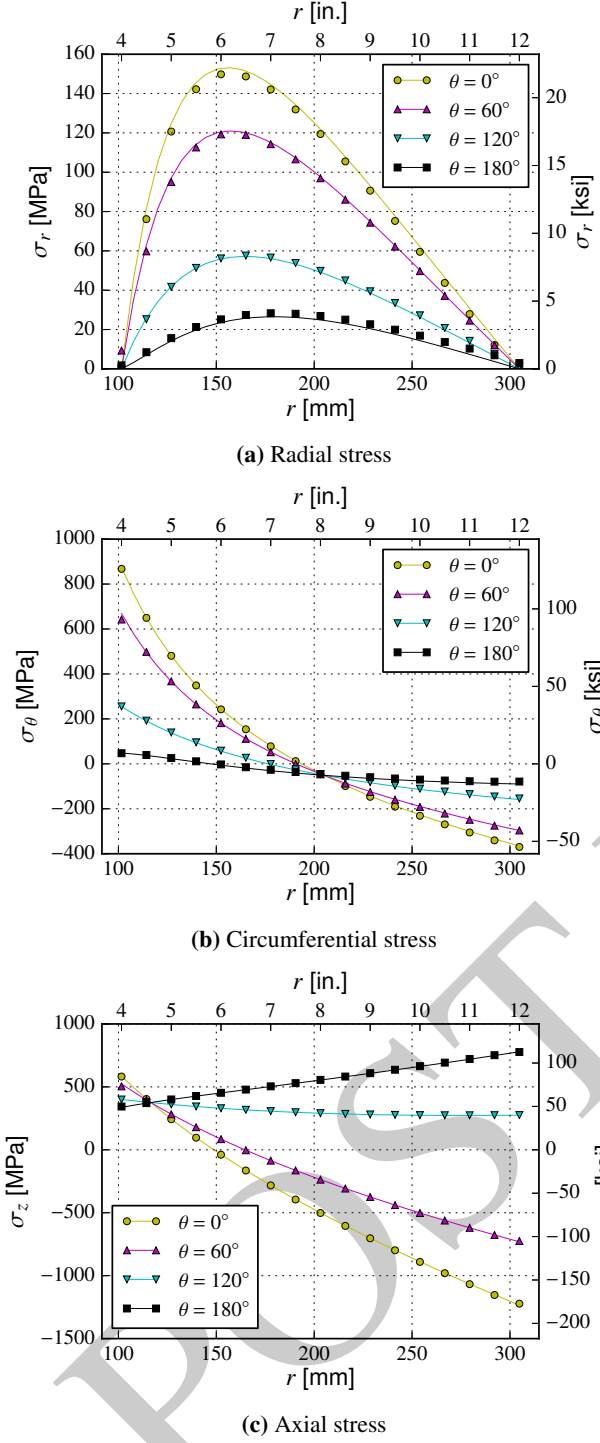


**Fig. 5:** Holms (1952): sample of (a) radial, (b) circumferential and (c) axial stress through the tube at  $\theta = 0^\circ, 60^\circ, 120^\circ$  and  $180^\circ$ ; solid lines denote results from Eqs. (18), (19) and (32) and markers denote results sampled from OpenFOAM®; compression is negative and tension is positive

the irradiated front side is annotated and a composition of the component stresses at this location can be found in Table 6 along with a calorific balance.

The tube efficiency  $\eta_t$  is defined here as the ratio of energy

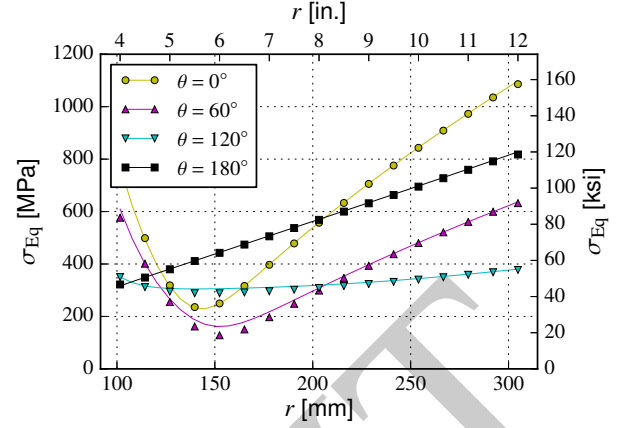


**Fig. 6:** Holms (1952) equivalent stress through the tube at  $\theta = 0^\circ, 60^\circ, 120^\circ$  and  $180^\circ$ ; solid lines denote results from Eqs. (18), (19) and (32) and markers denote results sampled from OpenFOAM®; Eq. (45) overpredicts equivalent stress at  $\theta = 0^\circ$  by more than a factor of three

**Tab. 5:** Heat transfer fluid and tube flow properties evaluated at a bulk fluid temperature of  $450^\circ\text{C}$  for DN25 tubes

Property	Units	Salt	Sodium
$\rho$	$\text{kg m}^{-3}$	1804	846
$c_p$	$\text{J kg}^{-1} \text{K}^{-1}$	1520	1272
$\mu$	$\text{mPa s}$	1.5	0.25
$k$	$\text{W m}^{-1} \text{K}^{-1}$	0.5	67
$\dot{m}$	$\text{kg s}^{-1}$	5	4
$U$	$\text{m s}^{-1}$	3.9	6.7
Re	$10^5$	1.44	6.67
$\Delta p$	$10^{-2} \text{ bar m}^{-1}$	-7.58	-7.74
Nu		548	19.6
$h_i$	$\text{kW m}^{-2} \text{K}^{-1}$	9.7	43.6
Bi		0.79	3.58

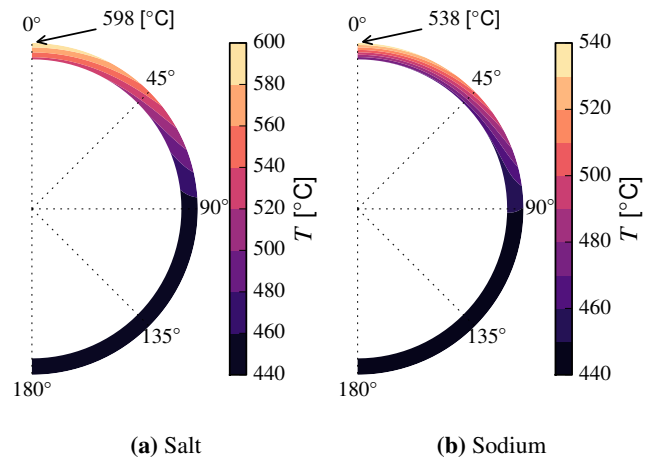


**Fig. 7:** Temperature for DN25 Sch. 5S UNS S31600 tubes irradiated with  $850 \text{ kW m}^{-2}$ ; peak temperature at outer tube front side annotated

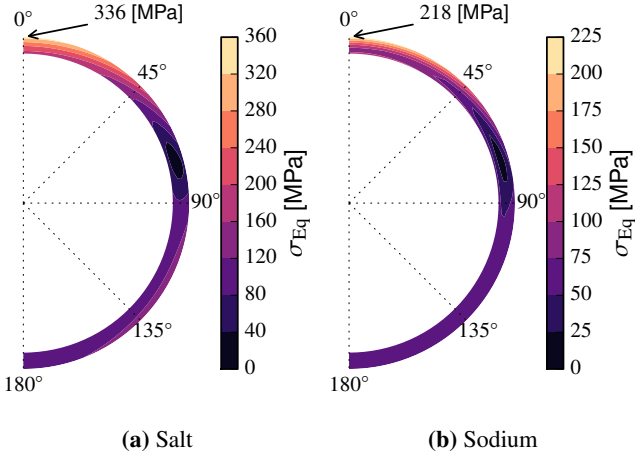


**Fig. 8:** Equivalent von Mises stress for DN25 Sch. 5S UNS S31600 tubes irradiated with  $850 \text{ kW m}^{-2}$  given the state of zero axial force from Eq. (32); peak stress at outer tube front side annotated

**Tab. 6:** Summary of heat balance for a metre of tube and resulting stress at the outer tube front side given the state of zero axial force

Result	Units	Salt	Sodium
$q_{\text{inc}}$	$\text{kW m}^{-1}$	-14.19	-14.19
$q_{\text{htf}}$	$\text{kW m}^{-1}$	12.08	12.21
$\eta_t$	%	85.11	86.05
$\sigma_r$	MPa	0	0
$\sigma_\theta$	MPa	-100.6	-108.8
$\sigma_z$	MPa	-374.2	-250.6
$\sigma_{\text{Eq}}$	MPa	336.0	218.0

incident on the tube to that which is transferred to the fluid as heat:

$$\eta_t = \left| \frac{\int_A q''_{\text{htf}} dA}{\int_A q''_{\text{inc}} dA} \right| \quad (54)$$

The tube efficiency reported in Table 6 is a local value for a segment of tube with a bulk fluid temperature of  $450^\circ\text{C}$ . The value is reasonably sensitive to external convective loss assumptions and whether the back side external wall is assumed adiabatic. For example, if the back side of the tube were considered adiabatic and external convection is reduced to  $20 \text{ W m}^{-2} \text{ K}^{-1}$ , the tube efficiency increases to 89.76% and 90.72%, and equivalent tube stress decreases to 330.4 MPa and 215.5 MPa for molten salt and liquid sodium respectively. Subject to the incident flux of  $850 \text{ kW m}^{-2}$  the tube efficiency for molten salt and sodium do not differ greatly.

Circumferential stress given in Table 6 for the outer tube front side is slightly higher for liquid sodium than it is for molten salt. The reason for this is the slightly higher absorbed power density at the tube front side in the case of sodium.

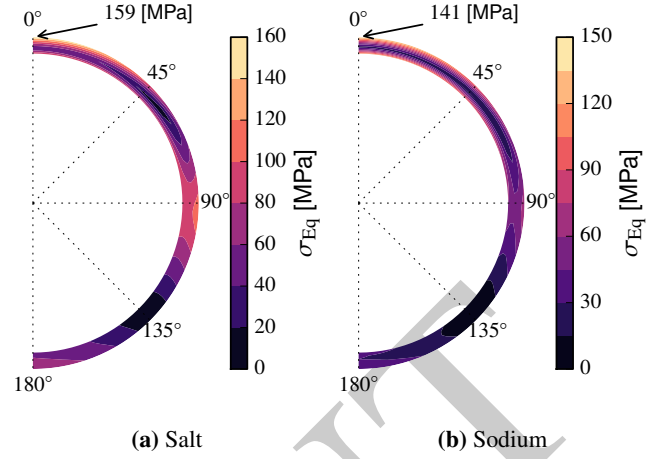


**Fig. 9:** Equivalent von Mises stress for DN25 Sch. 5S UNS S31600 tubes irradiated with  $850 \text{ kW m}^{-2}$  with the condition of annulled bending from Eq. (33); peak stress at outer tube front side annotated

Losses to the environment (convection and radiation) from liquid sodium tubes are smaller due to the lower front side tube temperature which results in more heat transferred to the fluid. This translates directly to a higher temperature difference between inside and outside tube surface at the front side, which results in higher circumferential stress.

Where the tubes with liquid sodium perform significantly better than those with molten salt is in regards to axial stress. Due to the lower overall front side tube temperature, the bending stress over the tube's cross section is smaller, such that when observing the equivalent tube stress of liquid sodium versus molten salt in Fig. 8, the difference between molten salt and liquid sodium peak tube stress is largely due to axial stress.

In some instances it is feasible to attach one end of the tube to its manifold using bellowed tube (Boerema, 2014) or otherwise allow unconstrained bending to alleviate axial stress. The reduction of stress on account of the tube's capacity to bend away from the flux is significant, as we see in Fig. 9 where Eq. (33) was used in place of Eq. (32) for the axial stress component.

To observe how the simple Babcock & Wilcox formula in Eq. (45) compares with predictions using the present method described in Sec. 2, the numbers for molten salt in Table 6 are given again with a separation of the axial and circumferential components from Eqs. (43) and (44) in Table 7. The difference in sign is ascribed to the fact that both axial and circumferential stress at the outer surface is compressive and thus negative. The present method resolves the sign correctly whereas the Babcock & Wilcox formula requires the user to be aware that the resolved stress is multi-axial. Orthogonal (multi-axial) stress components should ideally be considered separately, and only ever combined in something like the Mises or Tresca yield criterion<sup>15</sup>.

The circumferential component calculated by Eq. (44) is overpredicted because it uses the axisymmetrical assumption,

<sup>15</sup> And even then caution should be exercised.

and because calculation of the axial component is simplifying the nonaxisymmetrical geometrical temperature distribution, its impact is not accurately captured and the axial component calculated by Eq. (43) is underpredicted. The resulting value from Eq. (45) of 414.3 MPa is a significant overprediction when compared with the equivalent stress from Eq. (49) of 336.0 MPa. Questions could be raised surrounding Babcock & Wilcox (1984) claims to accuracy, however, given the fact that it will always overpredict the equivalent stress, confidence gained with its use in preliminary design screening can be improved upon in subsequent more detailed analysis.

**Tab. 7:** Comparison of stress components for molten salt DN25 Sch. 5S UNS S31600 tubes irradiated with  $850 \text{ kW m}^{-2}$  using the present method with Eq. (32) and the simple Babcock & Wilcox's formula from Kistler (1987) and Kolb (2011) without correction

Result	Units	Present method	Babcock & Wilcox's
$\sigma_r$	MPa	0	0
$\sigma_\theta$	MPa	-100.6	155.9
$\sigma_z$	MPa	-374.2	258.4
$\sigma_{Eq}$	MPa	336.0	225.3
Eq. (45)	MPa		414.3

In the following Secs. 5.1 to 5.3 we use the present method to observe the sensitivity of peak tube stress to fluid flow properties, tube properties and flux profile with parameter variation. Tornado charts are used to illustrate how much peak tube stress can vary with single parameters. To assist in clean presentation the base case internal convection coefficients have been rounded to the nearest  $\text{MW m}^{-2} \text{K}^{-1}$ : namely  $1 \text{ MW m}^{-2} \text{K}^{-1}$  for molten salt and  $4 \text{ MW m}^{-2} \text{K}^{-1}$  for liquid sodium. Shaded chart bar sections imply an increase in parameter and white bar sections imply a reduction, except in the instance of internal tube pressure and fouling factor in Sec. 5.1 where the starting point of the parameter variation is zero.

### 5.1. Fluid flow properties

Owing to its tensile contribution to equivalent stress, the addition of internal pressure initially decreases equivalent stress. At some point the addition of more internal pressure results in tensile hoop stress dominating, although this point depends heavily on the magnitude of compression due to thermal stress. The resulting maximum equivalent stress at the outer tube front side is shown in the top bars of the tornado chart in Fig. 10 for the interval of 5 and 10 MPa, already considerably higher than typical molten salt receiver pressures of 1.5 MPa to 2.5 MPa (Drake et al., 2014).

The impact of fouling or the addition of thermal insulation/resistance to the tube's inner surface on peak equivalent thermal stress is seen in the middle bars of Fig. 10. To liquid sodium we are adding the range for fouling found in literature (Foust, 1972), but to keep the illustration within reasonable bounds we have added a little more than half the range found in literature for molten salt (Zavoico, 2001; Rodríguez-Sánchez et al., 2014). With a fouling factor of  $8.808 \text{ m}^2 \text{K W}^{-1}$

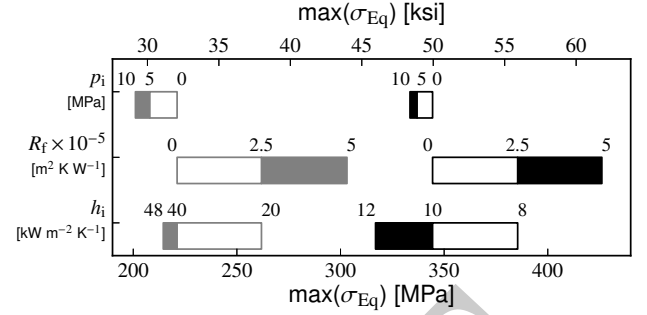


**Fig. 10:** Sensitivity of peak equivalent tube stress with molten salt (black) and liquid sodium (grey) to internal convection coefficient  $h_i$ , fouling factor  $R_f$  and internal pressure  $p_i$

the internal convection coefficient of molten salt is reduced according to Eq. (10) to around  $5 \text{ kW m}^{-2} \text{K}^{-1}$ , resulting in a 1.3% reduction in tube thermal efficiency and a peak thermal stress of 475.4 MPa. As indicated in Sec. 2.1.2, the phenomena of fouling is usually associated with the deposition of solubles from a hotter to a colder region in the heat transfer fluid cycle. How much fouling plays a role in the thermodynamics of receiver tubes is the topic of further investigation. The impact of any variance in inner convection coefficient alone on stress is shown in the lower bar.

### 5.2. Tube properties

Thermal expansion coefficient and Young's modulus are related in that the former controls the magnitude of thermal strain and the latter controls the body continuity's response to the strain. A reduction in either decreases stress as is illustrated in Fig. 11 and intuitively understood from Eqs. (18), (19) and (32).

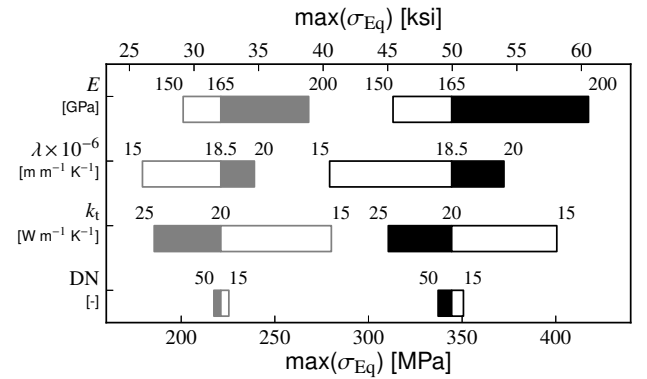


**Fig. 11:** Sensitivity of peak equivalent tube stress with molten salt (black) and liquid sodium (grey) to Young's modulus  $E$ , thermal expansion coefficient  $\lambda$ , tube conductivity  $k_t$  and nominal tube diameter  $DN$

Variation in tube conductivity impacts the temperature gradient for a given flux and thus the degree to which temperature difference is established across the body continuity. Just as thinner tube wall reduces the temperature difference between outside and inside tube surfaces, more gradual temperature gradients result in lower stress.



Selection of a material's elastic modulus, thermal expansion coefficient and thermal conductivity is unavoidably related. Nickel-chromium metals such as UNS N00230 with a particularly low thermal expansion coefficient are widely adopted, even though its modulus of elasticity is a little higher and its thermal conductivity is a little lower than that of S31600 at 450 °C.

Any change in tube size has an impact on internal convection coefficient unless mass flow is matched to ensure the same value is achieved. It was assumed that any change in DN size implied a matched change in mass flow to ensure that internal convection coefficient remained at  $1 \text{ MW m}^{-2} \text{ K}^{-1}$  for molten salt and  $4 \text{ MW m}^{-2} \text{ K}^{-1}$  for liquid sodium. The choice of tube diameter has a limited impact on peak equivalent stress at the outer front side by changing the distance through which the bending moment in axial stress is felt. The same thermal expansion at a greater distance to the cylindrical axis has a larger moment through which to move than if it were closer.

### 5.3. Flux profile

The intent of this final exploration is to illustrate the impact of flux profile on peak tube stress. Only idealised profiles are considered. The collimated incident flux density as shown in Fig. 1 was integrated over the tube's outer surface to provide the amount of sensible heat for the simple cosine 'base case'. A flux density profile provided in a recent Abengoa report (Drake et al., 2014) is included and is a close match to the simple cosine case. Two further case profiles with the same total flux (area under the curve) as the base case were considered. The first has the heat distributed evenly to the front side of the tube, and the second distributes the heat linearly from the front side to the back side. A fifth profile was considered in which the peak flux from the cosine distribution was distributed evenly to the front side of the tube. The five flux profiles are illustrated in Fig. 12 with the last three profiles receiving the names 'step', 'fade' and 'peak step' respectively.

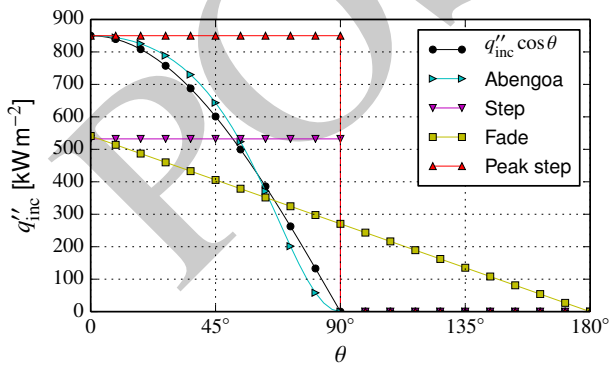


**Fig. 12:** Illustration of the five flux profiles considered: the common cosine flux density distribution, a profile used by Abengoa (Drake et al., 2014), two idealised profiles distributing the same amount of the heat from the cosine distribution to parts of the tube and one delivering the same peak flux as the cosine distribution to the front of the tube

A tabulation of peak tube stress for molten salt and liquid sodium tubes with the five flux profiles is given in Table 8.

**Tab. 8:** Peak equivalent tube stress  $\sigma_{Eg}$  in MPa for the four differing flux cases indicated in Fig. 12: base case is also given for the adiabatic tube back side

Case	Salt	Sodium
Base	336.0	218.0
Abengoa	338.0	218.8
Step	175.5	127.1
Fade	168.7	120.2
Peak step	280.8	205.5

It is little surprise that the first two cases are similar as the tube's temperature distribution varies little between them. While we might expect in the case of the two equal energy flux density profiles (step, fade) that a significantly lower peak tube stress would be observed on account of the lower peak tube flux value, it is surprising to discover that if the peak flux of the step profile is increased to be the same as that of the base case ( $850 \text{ kW m}^{-2}$ ) - effectively doubling the heat transferred to the fluid - peak tube stress would still be lower at 280.8 MPa for molten salt and 205.5 MPa for liquid sodium. This demonstrates that while peak flux is an important factor in determining peak equivalent tube stress, the distribution of flux around the tube's circumference is just as critical.

## 6. Conclusions

Peak thermal stress is a major limitation when trying to achieve high flux on tubular receivers. Ignoring axial stress (as some authors have) leads to incorrect conclusions regarding the maximum allowable flux on tubular receivers, as does using certain simple thermal stress calculations. The present work has unified some classical methods for the steady-state analytical calculation of thermoelastic stress in concentrating solar thermal receiver tubes. Particular attention has been given to the correct calculation of the axial stress component given the typical states in which receiver tubes may be configured. In nonaxisymmetrically heated tubes, axial stress is always the dominant stress component in the equivalent stress criteria.

Peak thermal stress in tubular receivers is dependent on the conductivity of the heat transfer fluid used. Higher conductivity of heat transfer fluid results in a higher convective coefficient and lower tube temperatures. The lower front side tube temperature reduces axial stress by decreasing the temperature difference between irradiated tube front side and concealed tube back side. In the comparison of typical state-of-the-art molten salt receiver tubes with tubes utilising liquid sodium, it is shown that peak thermal stress can be reduced by 35%.

By way of parameter studies it is shown how certain tube flow properties impact peak thermal stress. Peak thermal stress at the outer tube front side surface is compressive, which when superimposed with expected values of tensile pressure stress results in lower peak stress at the tube front side. Should fouling

occur in the receiver tubes, peak thermal stress is increased due to the increase in tube temperature at the irradiated tube front side.

The choice of tube material impacts peak thermal stress in multiple ways. Any increase in Young's modulus of elasticity or coefficient of thermal expansion increases a material's peak thermal stress for a given solar flux. An increase in the thermal conductivity of a chosen tube material has the capacity to reduce peak thermal stress. While a larger nominal tube size can marginally decrease peak thermal stress, the impact this selection has on convection coefficient must also be considered.

Through the use of some idealised flux profiles it is shown that the non-uniformity of flux plays an important roll in peak thermal stress. A more uniform distribution of flux on the tube's surface results in a significant reduction in peak thermal stress.

## 7. Acknowledgements

Many of the findings presented in this paper draws on research performed as part of the Australian Solar Thermal Research Initiative (ASTRI), a project supported by the Australian Government, through the Australian Renewable Energy Agency (ARENA). Responsibility for the views, information or advice expressed herein is not accepted by the Australian Government. The corresponding author is supported by an Australian Postgraduate Award (APA) and would like to thank Ildo Agnetti at CMI Solar and James Fisher at Vast Solar for their contributions.

## References

- ASME, 2007. Boiler and Pressure Vessel Code. American Society of Mechanical Engineers. New York.
- Babcock & Wilcox, 1984. Molten Salt Receiver Subsystem Research Experiment, Phase I - Final Report. Technical Report SAND82-8178. Babcock & Wilcox Company. Barberton, OH. URL: <https://ntrl.ntis.gov/NTRL/dashboard/searchResults/titleDetail/DE85002669.xhtml>.
- Besarati, S., Goswami, D., 2017. Advances in Concentrating Solar Thermal Research and Technology. Woodhead Publishing, chapter 8 – Supercritical CO<sub>2</sub> and other advanced power cycles for concentrating solar thermal (CST) systems. pp. 157–178. doi:10.1016/B978-0-08-100516-3.00008-3.
- Bijlaard, P.P., Dohrmann, R.J., Duke, J.M., 1968. Thermal stress analysis of nonuniformly heated cylindrical shell and its application to a steam generator membrane wall. J. Eng. Power 90, 73–81. doi:10.1115/1.3609137.
- Boerema, N., 2014. Fundamental investigation into the design and operation of a high flux sodium receiver. Ph.D. thesis. UNSW. URL: <http://handle.unsw.edu.au/1959.4/54364>.
- Boley, B.A., Weiner, J.H., 1960. Theory of Thermal Stresses. Wiley, New York.
- Chavez, J.M., Smith, D.C., 1992. A final report on the phase I testing of a molten-salt cavity receiver: volume II – the main report. Technical Report SAND87-2290. Sandia National Laboratories. Albuquerque. doi:10.2172/5042358.
- Coventry, J., Andraka, C., Pye, J., Blanco, M., Fisher, J., 2015. A review of sodium receiver technologies for central receiver solar power plants. Sol. Energy 122, 749–762. doi:10.1016/j.solener.2015.09.023.
- Drake, T., Bruce, K., Burkholder, F., 2014. Baseload nitrate salt central receiver power plant design. Technical Report DOE-ABENGOA-3596. Abengoa Solar LLC. Lakewood, CO. doi:10.2172/1165353.
- Falcone, P.K., 1986. A handbook for solar central receiver design. Technical Report SAND86-8009. Sandia National Laboratories. Livermore. doi:10.2172/6545992.
- Faupel, J., Fisher, F., 1981. Engineering Design: A Synthesis of Stress Analysis and Material Engineering. John Wiley and Sons.
- Fink, J.K., Leibowitz, L., 1995. Thermodynamic and Transport Properties of Sodium Liquid and Vapor. Technical Report ANL/RE-95/2. Reactor Engineering Division, Argonne National Laboratory. Chicago. doi:10.2172/94649.
- Fork, D.K., Fitch, J., Ziaei, S., Jetter, R.I., 2012. Life estimation of pressurized-air solar-thermal receivers tubes. J. Sol. Energy Eng. 134, 041016. doi:10.1115/1.4007686.
- Foust, O.J. (Ed.), 1972. Sodium-NaK Engineering Handbook. Gordon and Breach, Science Publishers, Inc.
- Gatewood, B.E., 1941. Thermal stresses in long cylindrical bodies. Philos. Mag. 32, 282–301. doi:10.1080/1478644108521303.
- Goodier, J.N., 1937a. Thermal stress. J. Appl. Mech. 4, 33–36.
- Goodier, J.N., 1937b. Thermal stress in long cylindrical shells due to temperature variation round the circumference, and through the wall. Can. J. Res. 15, 49–58.
- Goodier, J.N., 1957. Thermal stresses and deformation. J. Appl. Mech. 24, 467–474.
- Gupta, G.D., Rao, M.S.M., Narayanan, T.V., Gangadharan, A.D., 1978. Thermoelastic analysis of nonaxisymmetrically heated thick cylindrical shells. J. Pressure Vessel Technol. 100, 107–111. doi:10.1115/1.3454421.
- Hetnarski, R.B., Eslami, M.R., 2009. Thermal Stress – Advanced Theory and Applications. Springer.
- Ho, C.K., Mahoney, A.R., Ambrosini, A., Bencomo, M., Hall, A., Lambert, T.N., 2013. Characterization of Pyromark 2500 for high-temperature solar receivers. J. Sol. Energy Eng. 136, 014502. doi:10.1115/1.4024031.
- Holman, J.P., 1997. Heat Transfer. 8<sup>th</sup> ed., McGraw-Hill, Inc.
- Holms, A.G., 1952. A biharmonic relaxation method for calculating thermal stress in cooled irregular cylinders. Technical Report NACA-TR-1059. Lewis Flight Propulsion Lab. Cleveland. URL: <https://ntrs.nasa.gov/search.jsp?R=19930092105>.
- Incropera, F.P., Dewitt, D.P., Bergman, T.L., Lavine, A.S., 2006. Fundamentals of Heat and Mass Transfer. 6<sup>th</sup> ed., John Wiley & Sons.
- Kim, J.S., Potter, D., Gardner, W., Soo Too, Y.C., Padilla, R.V., 2016. Ideal heat transfer conditions for tubular solar receivers with different design constraints, in: 22nd Annual SolarPACES Conference, Abu Dhabi. doi:10.1063/1.4984373.
- Kistler, B.L., 1987. Fatigue analysis of a solar central receiver design using measured weather data. Technical Report SAND86-8017. Sandia National Laboratories. Albuquerque. URL: <https://ntrl.ntis.gov/NTRL/dashboard/searchResults/titleDetail/DE87008886.xhtml>.
- Kiusalaas, J., 2010. Numerical Methods in Engineering with Python. 2nd ed., Cambridge University Press.
- Kolb, G.J., 2011. Evaluation of possible next-generation high-temperature molten-salt power towers. Technical Report SAND2011-9320. Sandia National Laboratories. Albuquerque. URL: 10.2172/1035342.
- Liao, Z., Li, X., Xu, C., Chang, C., Wang, Z., 2014. Allowable flux density on a solar central receiver. Renewable Energy 62, 747–753. doi:10.1016/j.renene.2013.08.044.
- Logie, W.R., Asselineau, C.A., Pye, J.D., Coventry, J., 2015. Temperature and heat flux distributions in sodium receiver tubes, in: APVI Asia-Pacific Solar Research Conference, Brisbane.
- Logie, W.R., Pye, J.D., Coventry, J., 2016. Thermal elastic stress in sodium receiver tubes, in: APVI Asia-Pacific Solar Research Conference, Canberra.
- Luo, Y., Du, X., Yang, L., Xu, C., Yang, Y., 2014. Study on the allowable flux density for a solar central dual-receiver, in: 20th Annual SolarPACES Conference, Beijing. doi:10.1016/j.egypro.2015.03.017.
- Marocco, L., Alberti di Valmontana, A., Wetzel, T., 2016. Numerical investigation of turbulent aided mixed convection of liquid metal flow through a concentric annulus. Int. J. Heat Mass Transfer 105, 479–494. doi:10.1016/j.jheatmasstransfer.2016.09.107.
- Marugán-Cruz, C., Flores, O., Santana, D., García-Villalba, M., 2016. Heat transfer and thermal stresses in a circular tube with a non-uniform heat flux. Int. J. Heat Mass Transfer 96, 256–266. doi:10.1016/j.jheatmasstransfer.2016.01.035.
- Michell, J.H., 1899. On the direct determination of stress in an elastic solid, with application to the theory of plates. Proc. London Math. Soc. 31, 100–124. doi:10.1112/plms/s1-31.1.100.
- Narayanan, T.V., Gupta, G.D., Rao, M.S.M., 1979. Structural design of a superheater for a central solar receiver. J. Pressure Vessel Technol. 101, 2–9.

- doi:[10.1115/1.3454595](https://doi.org/10.1115/1.3454595).
- Neises, T., Wagner, M.J., Gray, A.K., 2014. Structural design considerations for tubular power tower receivers operating at 650°C, in: ASME 8th Int. Conference on Energy Sustainability, Boston, Massachusetts. doi:[10.1115/ES2014-6603](https://doi.org/10.1115/ES2014-6603).
- Nithyanandam, K., Pitchumani, R., 2016. Thermal and structural investigation of tubular supercritical carbon dioxide power tower receivers. *Sol. Energy* 135, 374–385. doi:[10.1016/j.solener.2016.05.039](https://doi.org/10.1016/j.solener.2016.05.039).
- Pacheco, J.E., Ralph, M.E., Chavez, J.M., Dunklin, S.R., Rush, E.E., Ghanbari, C.M., Matthews, M.W., 1995. Results of molten salt panel and component experiments for solar central receivers: cold fill, freeze/thaw, thermal cycling and shock, and instrumentation. Technical Report SAND94-2525. Sandia National Laboratories. Albuquerque. doi:[10.2172/46671](https://doi.org/10.2172/46671).
- Pacio, J., Marocco, L., Wetzol, T., 2015. Review of data and correlations for turbulent forced convective heat transfer of liquid metals in pipes. *Heat Mass Transfer* 51, 153–164. doi:[10.1007/s00231-014-1392-3](https://doi.org/10.1007/s00231-014-1392-3).
- Pacio, J., Singer, C., Wetzol, T., Uhlig, R., 2013. Thermodynamic evaluation of liquid metals as heat transfer fluids in concentrated solar power plants. *Appl. Therm. Eng.* 60, 295–302. doi:[10.1016/j.applthermaleng.2013.07.010](https://doi.org/10.1016/j.applthermaleng.2013.07.010).
- Pomeroy, B.D., Fleck, J.J., Marsh, W.D., Brown, D.H., Shah, R.P., 1978. Comparative study and evaluation of advanced-cycle systems. Technical Report EPRI-AF-664 (Vol.1). General Electric Co., Schenectady, NY. doi:[10.2172/6889622](https://doi.org/10.2172/6889622).
- Pye, J.D., Zheng, M., Zapata, J., Asselineau, C.A., Coventry, J., 2014. An energy analysis of tubular solar-thermal receivers with different working fluids, in: 20th Annual SolarPACES Conference, Beijing.
- Rao, M.S.M., Narayanan, T.V., Gupta, G.D., 1979. Inelastic analysis of nonaxisymmetrically heated thick cylindrical shells. *J. Pressure Vessel Technol.* 101, 235–241. doi:[10.1115/1.3454628](https://doi.org/10.1115/1.3454628).
- Rodríguez-Sánchez, M.R., Soria-Verdugo, A., Almendros-Ibáñez, J.A., Acosta-Iborra, A., Santana, D., 2014. Thermal design guidelines of solar power towers. *Appl. Therm. Eng.* 63, 428–438. doi:[10.1016/j.applthermaleng.2013.11.014](https://doi.org/10.1016/j.applthermaleng.2013.11.014).
- Romero, M., González-Aguilar, J., 2017. Advances in Concentrating Solar Thermal Research and Technology. Woodhead Publishing. chapter 7 –Next generation of liquid metal and other high-performance receiver designs for concentrating solar thermal (CST) central tower systems. pp. 129–154. doi:[10.1016/B978-0-08-100516-3.00007-1](https://doi.org/10.1016/B978-0-08-100516-3.00007-1).
- Sánchez-González, A., Rodríguez-Sánchez, M.R., Santana, D., 2017. Aiming strategy model based on allowable flux densities for molten salt central receivers. *Sol. Energy* 157, 1130–1144. doi:[10.1016/j.solener.2015.12.055](https://doi.org/10.1016/j.solener.2015.12.055).
- Siebers, D.L., Kraabel, J.S., 1984. Estimating convective energy losses from solar central receivers. Technical Report SAND84-8717. Sandia National Laboratories. Albuquerque. doi:[10.2172/6906848](https://doi.org/10.2172/6906848).
- Skupinski, E., Tortel, J., Vautrey, L., 1965. Détermination des coefficients de convection d'un alliage sodium-potassium dans un tube circulaire. *Int. J. Heat Mass Transfer* 8, 937–951. doi:[10.1016/0017-9310\(65\)90077-3](https://doi.org/10.1016/0017-9310(65)90077-3). in French. English title: Determination of convection coefficient for a sodium-potassium alloy in a circular tube.
- Timoshenko, S., Goodier, J.N., 1951. *Theory of Elasticity*. 2nd ed., McGraw-Hill Book Company, Inc. 1st ed. 1934.
- Tuković, Z., Cardiff, P., Karač, A., Jasak, H., Ivanković, A., 2014. Openfoam library for fluid structure interaction, in: 9th OpenFOAM Workshop, Zagreb, Croatia.
- Vant-Hull, L.L., 2002. The role of “allowable flux density” in the design and operation of molten-salt solar central receivers. *J. Sol. Energy Eng.* 124, 165–169. doi:[10.1115/1.1464124](https://doi.org/10.1115/1.1464124).
- Winter, C.J., Sizmann, R.L., Vant-Hull, L.L. (Eds.), 1991. *Solar Power Plants*. Springer-Verlag.
- Young, W.C., Budynas, R.G., 2002. *Roark's Formulas for stress and strain*. 7th ed., McGraw-Hill, Inc.
- Zavoico, A.B., 2001. Solar power tower design basis document. Technical Report SAND2001-2100 Rev 0. Sandia National Laboratories. California. doi:[10.2172/786629](https://doi.org/10.2172/786629).